The influence of fluid-structure interaction on cloud cavitation about a hydrofoil

[1]Samuel M Smith*; [1]James A Venning; [1]Paul A Brandner; [1]Bryce W Pearce; [1]Dean R Giosio; [2]Yin Lu Young

[1]*Cavitation Research Laboratory, Australian Maritime College, Launceston, Tasmania, Australia*

[2]*Department of Naval Architecture and Marine Engineering, University of Michigan, Ann Arbour, MI, USA*

Abstract

The dynamics of cloud cavitation about rigid and flexible 3D hydrofoils is investigated in a cavitation tunnel. The two hydrofoils have identical undeformed geometry of tapered planform, NACA-0009 section and cantilevered setup at the hydrofoil root. The rigid model is made of stainless steel and the flexible model of carbon and glass-fibre reinforced epoxy resin with an effectively quasi-isotropic lay-up without material bend-twist coupling. Tests were conducted at a fixed incidence of 6°, a chord-based Reynolds number of 0.7×10^6 and a cavitation number ranging from 1.0 to 0.2. Unsteady force measurements were made simultaneously with high-speed imaging to enable correlation of forces and with cavity dynamics. High-resolution force spectra at discrete cavitation numbers and separate pressure sweeps were taken to acquire spectrograms of frequency response as a function of cavitation number. Three shedding modes, designated as types 1, 2 and 3, are apparent for both rigid and flexible hydrofoils although significant differences in peak amplitudes were observed. Types 2 and 3 shedding occur at high cavitation numbers where frequency varied with cavitation number and high-speed imaging showed the dominant shedding mechanism to be due to re-entrant jet formation. The type 1 shedding that developed with reduction in cavitation number, once cavity lengths grew to about full-chord, occurred at a nominally constant frequency. In this case, the imaging showed the dominant mechanism to be shockwave formation. This behaviour has been reported upon extensively in literature although there are some new features apparent from the data. The flexibility of the composite hydrofoil was found to increase the magnitude of the force fluctuations for the low frequency type 1 mode compared to the rigid hydrofoil. However, hydrofoil flexibility was seen to dampen the fluctuating magnitude of the high-frequency type 2 and 3 modes, despite being close to the hydrofoil's natural frequency.

Keywords: Fluid-structure interaction; Cloud cavitation; Hydrofoil

Introduction

The adverse effects of cavitation on hydrofoils, such as unsteady loading and induced vibration due to the shedding of cloud cavitation, can be delayed and mitigated through utilizing passive control of the 3-D morphology. Recent research on these self-adaptive properties of lifting surfaces has been carried out on composite propellers [1,2] and active control surfaces [3]. Geometric aspects of hydrofoils, such as skew and pitch, can be passively tailored allowing for the suppression or delay of cavitation on propellers operating in unsteady inflows [4].

The effects of unsteady cloud cavitation on the hydroelastic response of hydrofoils has previously been investigated [5] with Akcabay et al. [6] showing that greater spanwise flexibility of isotropic hydrofoils with the centre of pressure upstream of the shear centre causes increased cavity length, reduced shedding frequency and broadening of the induced vibration frequencies. Depending on the flow conditions, several possible mechanisms have been identified as the primary instability causing periodic shedding. These include re-entrant jet formation [7-10], shockwave propagation [9-14] and growth of interfacial instabilities such as Kelvin-Helmholtz waves [15]. In a recent study on cloud cavitation about a sphere, all three mechanisms have been observed occurring either under varying flow conditions or as a complex coupled mechanism [13]. Each of these instabilities have certain flow conditions in which they become the critical driver of shedding in cloud cavitation, resulting in the formation of two distinct modes [16]. The low-frequency (type 1) mode, typically defined as transitional cavity oscillation, occurs at relatively low cavitation number to incidence ratios ($\sigma/2\alpha$) where the long cavity is periodically shed due to shockwave propagation generated from the collapse of a previously shed cavity. The shedding frequency of the type 1 mode is typically independent of $\sigma/2\alpha$, occurring at chord-based Strouhal numbers, St, between 0.15-0.3. The type 2 mode, typically defined as partial cavity instability, occurs at higher $\sigma/2\alpha$, where a re-entrant jet is the cause of periodic shedding with its frequency changing with σ due to cavity length dependence on σ.

Fluid-structure interaction (FSI) between cloud cavitation and hydrofoils is an intricate phenomenon due to complex interactions between turbulent flow structures, phase-change dynamics, and the structural response of

*Corresponding Author, Samuel Smith: ssmith18@utas.edu.au

the hydrofoil (Figure 1). To investigate this phenomena, we present force measurements with synchronised high-speed photography, providing insight into the spectral content of unsteady force oscillations. The data obtained also sheds light on the disparity in some previous findings as discussed in [17]. The aim of this study is to further the understanding of cloud cavitation about a 3D hydrofoil and how FSI can influence its behaviour by assessing the correlation between the cavity dynamics and forces.

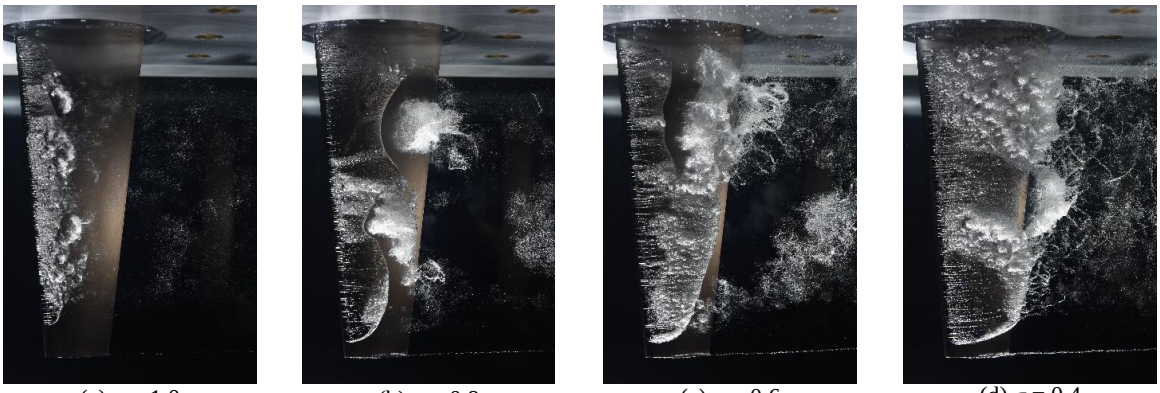

(a) $\sigma = 1.0$ (b) $\sigma = 0.8$ (c) $\sigma = 0.6$ (d) $\sigma = 0.4$

Figure 1 Photographs of the cloud cavitation about a stainless steel NACA-0009 hydrofoil with variations in σ at $\alpha = 6°$ and $Re = 0.7 \times 10^6$.

Experimental overview

The geometry and the mechanical properties of the hydrofoil models were selected based on modelling the static and dynamic fluid-structure interaction representative of propellers and control surfaces. Measurements were conducted using a flexible composite hydrofoil and a nominally rigid steel hydrofoil. The chosen geometry was a symmetric trapezoidal planform of 300 mm span (s) with a chord of 60 mm at the tip and 120 mm at the root, providing a geometric aspect ratio of 3.33 without considering the double body effect provided by the fixed well at the root. The chord length was chosen to be compatible with the mounting to the water tunnel test section and to achieve a chord-based Reynolds number, $Re_c = U_\infty c/\nu = 0.7 \times 10^6$ with $c = 90$ mm as the mean chord, which is representative of full scale applications. The geometry, in conjunction with a span-wise alignment of the fibre orientation, was intentionally chosen to principally consider bending deformation only of the flexible hydrofoil. A modified NACA-0009 section profile with a thicker trailing edge was selected for improved manufacture of the flexible composite model (see [18] for further details). Deflection measurements [18] showed that the maximum tip bending deflection of the flexible hydrofoil was 15% of the mean chord and negligible twist deformation, while the stainless steel hydrofoil was nominally rigid. The force data for the stainless steel model was found to be nominally invariant with Reynolds number for $\alpha \leq 6°$.

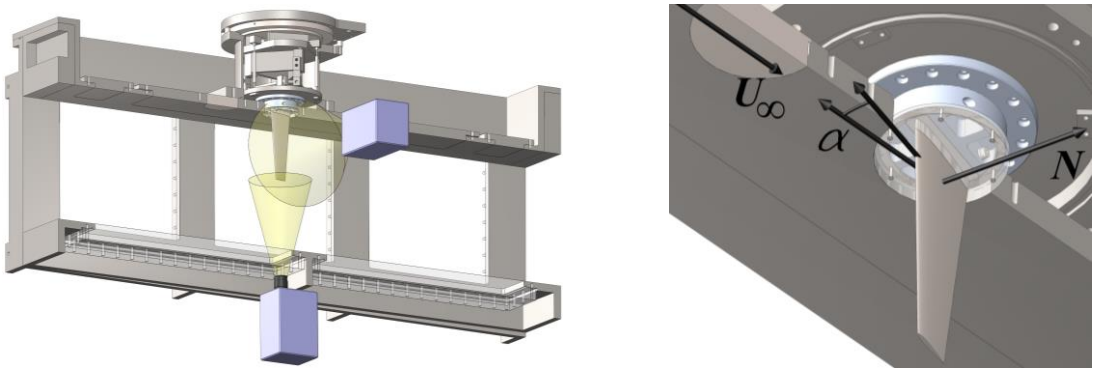

Figure 2 (Left) Section view of the experimental setup where the model hydrofoils are mounted via a 6-component force balance while the cavitation behaviour and tip deflection are imaged using two high-speed cameras. Tip deflection data is presented in [8]. (Right) A close-up of the hydrofoil showing the coordinate system used.

The flexible (composite) model was manufactured as a carbon/glass-epoxy hybrid structure with the lay-up sequence that yield quasi-isotropic response. The construction procedure is detailed in [18]. The nominally rigid (stainless steel) model was machined from a 316 grade stainless steel billet. First mode natural frequencies were obtained in air at 96 Hz and 112 Hz, and in water at 54 and 40 Hz for the stainless steel (rigid) and composite (flexible) models, respectively, determined from impact tests and hydrofoil loading spectra [18].

*Corresponding Author, Samuel Smith: ssmith18@utas.edu.au

Measurements were carried out in the Cavitation Research Laboratory water tunnel at the Australian Maritime College. The tunnel test section is 0.6 m square by 2.6 m long, in which the operating velocity and pressure ranges are 2 to 12 m/s and 4 to 400 kPa absolute, respectively. The tunnel volume is 365 m^3 of demineralised water. A detailed description of the facility is given in [19]. Two profiled plates were used to clamp the model within a housing that was attached to a 6-component force balance (Figure 2) with estimated precision of less than 0.1% on all components. Further description of the mounting arrangement may be found in [8]. Data was obtained for cavitation numbers from 1.0 to 0.2 and at a Reynolds number of 0.7×10^6 and an incidence of 6°. The hydrofoil tip cavitation number is defined as $\sigma = 2(p_\infty - p_v)/\rho U^2_\infty$, where p_∞ is the static pressure at the test section centreline, p_v is the vapour pressure, ρ is the water density and U_∞ is the test section velocity.

The cavitation behaviour was recorded using high-speed photography with a HighSpeedStar8 (LaVision, Germany) camera set up as shown in Figure 2. A Nikkor f/1.4 50 mm lens was used resulting in a magnification factor of 3.28 px/mm. High-speed images were recorded with a spatial resolution of 1024×1024 for 1 s at 7,000 Hz for the rigid hydrofoil while the flexible hydrofoil was recorded for 5 s at 1,000 Hz (due to synchronisation compatibility of the two cameras) to allow tip deflection measurements for data presented in [8]. The high-speed photography was synchronized with the force measurement acquisition by simultaneous triggering. Force and tunnel flow data were sampled at 7,000 Hz and 1,000 Hz, respectively.

Results and Discussion

High-resolution spectra of the hydrofoil normal force (perpendicular to the planform as shown in Figure 2) are presented in Figure 3 for all σ. Spectra were obtained using the Power Spectral Density (PSD) derived with the Welch estimate of the PSD [20] utilizing a window size of 4096 samples (4.1 s) and overlap of 256 samples (0.26 s). At each σ, both the rigid and flexible hydrofoils exhibited similar peak frequencies. As σ decreases, the frequency at which these peaks occur reduces due to the increasing cavity length requiring greater time for the cavity to grow and detach. It was also observed that there is an increase in the peak frequency amplitude by approximately one order of magnitude for every 0.2 reduction in σ (note the changing vertical scale in Figure 3).

Comparing the force spectra from both models, it is evident that the amplitude of the rigid hydrofoil is approximately double that of the flexible at σ = 0.8 and 0.6 for the peak frequencies. However, at σ = 0.4, the amplitude of the flexible is more than 3 times that of the rigid. The small differences at σ = 1.0, noting the scale of the PSD, is negligible. The horizontal axis is the cavity shedding frequency (*f)* Strouhal number defined using the mean chord, $St = fc/U_\infty$. Inconsistencies between rigid and flexible hydrofoil *St* is attributed to varying flow velocity between runs to maintain a constant Re_c at different temperatures. The 135 Hz (*St* = 1.43) peaks are associated with the structural response of the force balance based on previous experiments [21] and is evident in that the peaks occur at the same frequency for all σ.

At σ = 0.8, the common 37 Hz (*St* = 0.39) peak is linked to the periodic shedding of cloud cavitation from the upper half of the hydrofoil as seen in Figure 1(b). The secondary peaks at 42 and 49 Hz (*St* = 0.44 and 0.52) for the flexible and rigid hydrofoil, respectively, are attributable to the presence of another shedding event on the lower half of the span evident in the power distribution maps (Figure 5) discussed below.

Through measuring the normal force on the hydrofoils while the pressure is gradually increased, a joint time-frequency analysis (JTFA) can be conducted to investigate spectral characteristics at fine σ increments. The JTFA spectrograms shown in Figure 4 are obtained from 256 individual PSD spectra based on time series with 2048 samples (2 s) each and overlap of 1024 (1 s). Overlaying the high-resolution PSDs from Figure 3, good correspondence between the pressure sweep and steady state condition tests is observed showing the transient nature of the JTFA does not influence the resulting spectra. The pressure sweep was conducted both by increasing and decreasing σ and revealed no evidence of hysteresis.

Three trends are evident in the spectrograms corresponding to differing cloud cavitation shedding mechanisms discussed in the introduction. A shockwave-driven (type 1) mode occurs at $St \approx 0.1$ and within a range of σ from 0.3 – 0.55 for both hydrofoils. A slight dependence on σ is observed in both cases with the frequency increasing slightly with σ. A similar trait observed in [17] attributing it to low dissolved oxygen levels (≈ 7 ppm) where current results are for a constant dissolved oxygen level of about 3 ppm. Comparing the hydrofoils, the flexible model exhibits significantly greater amplitude than the rigid for virtually the entire type 1 mode region. As σ increases from 0.2, the flexible hydrofoil reaches its maximum at $\sigma \approx 0.38$, compared to $\sigma \approx 0.45$ for the rigid. As

*Corresponding Author, Samuel Smith: ssmith18@utas.edu.au

σ increases to approximately 0.5, the cavity becomes smaller, closing further upstream from the hydrofoil trailing edge. This reduction in cavity size causes a change in the pressure distribution and the resulting unsteady forces acting on the hydrofoil. With the cavity closing on the hydrofoil, a re-entrant flow may form (evident in Figure 1), becoming the primary shedding instability mechanism as σ increases.

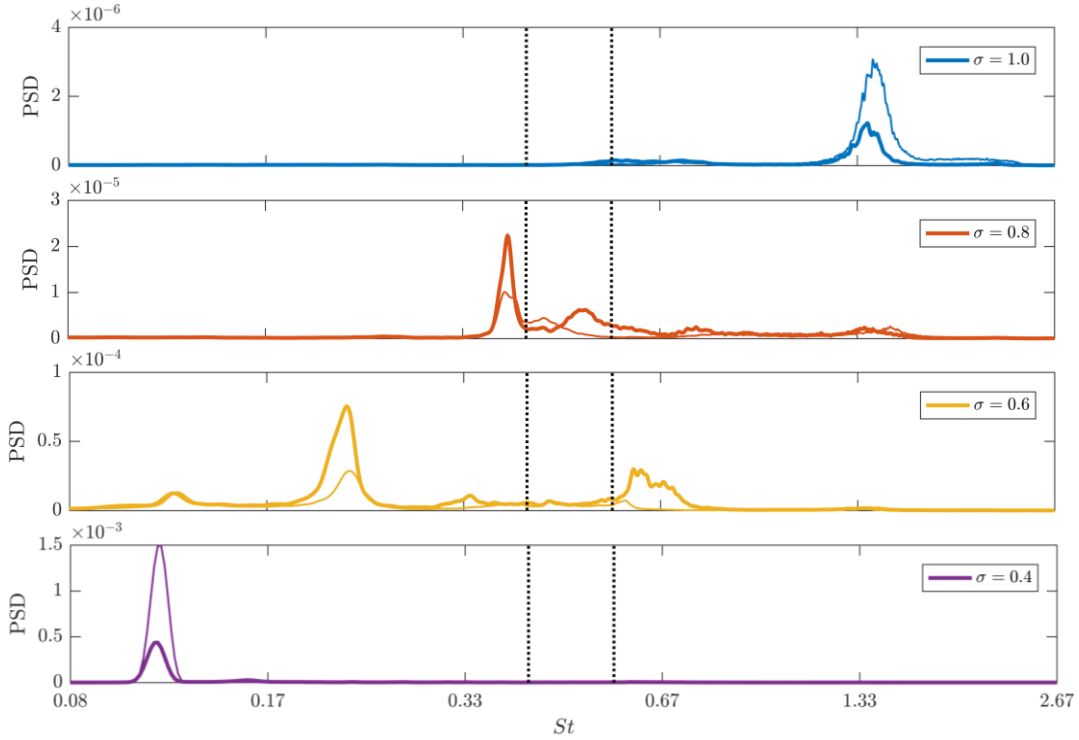

Figure 3 High-resolution non-dimensional normal-force spectra for the rigid (thick line) and flexible (thin line) hydrofoils for various σ. The vertical dashed lines show the flexible and rigid hydrofoils wetted natural frequencies. Note the ordinate axis limits change for each σ.

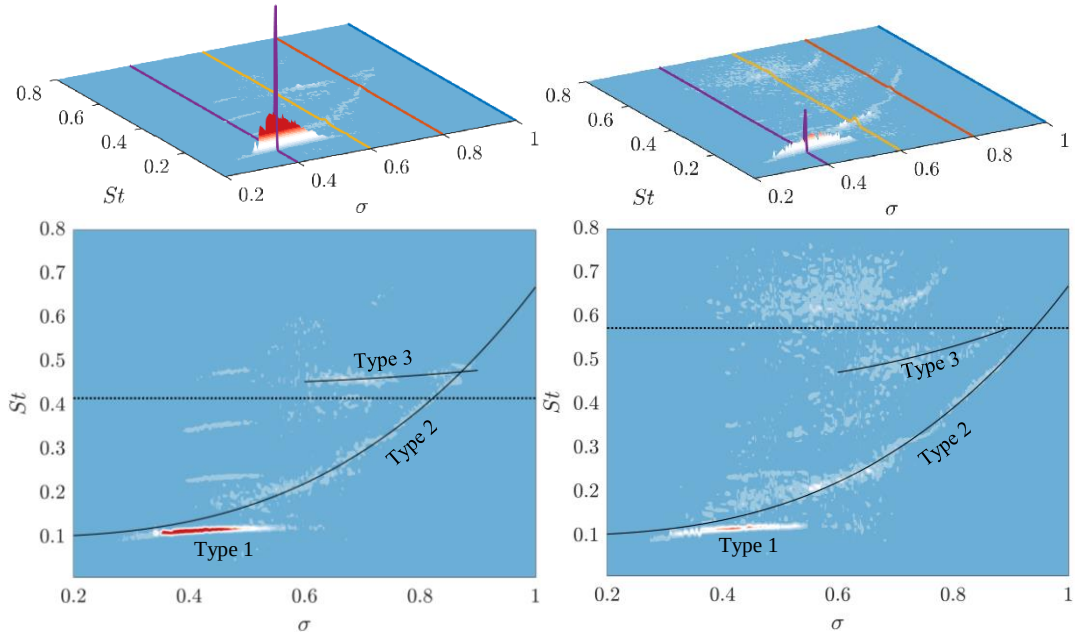

Figure 4 (Top) Isometric overlay of high-resolution spectra and low resolution spectrograms. (Bottom) Top view of the spectrograms with identified shedding modes and hydrofoil wetted natural frequency (dotted line). The left and right columns are data for the flexible and rigid hydrofoils, respectively. The results show convergence of type 2 into type 3 shedding modes with decreasing σ. Type 2 and 3 mode shedding frequencies varies as a power law with σ where $St_2 \approx 0.57\sigma^3 + St_1$, $St_{3F} \approx 0.05\sigma^3 + 0.44$ and $St_{3R} \approx 0.2\sigma^3 + 0.43$, where the subscripts are the shedding modes.

The type 2 mode, driven by re-entrant flow, follows an almost identical trend for both hydrofoils, showing strong dependence on σ and diminishing by $\sigma \approx 0.9$. Figure 4 shows the type 2 mode varies with σ as a power law with an exponent of 3 where $St_2 \approx 0.57\sigma^3 + St_1$, where the subscripts are the shedding modes. From approximately σ =

*Corresponding Author, Samuel Smith: ssmith18@utas.edu.au

0.5 to 0.6, types 1 and 2 modes co-exist, indicating that shedding-induced unsteady forces may be due to either re-entrant flow, shockwave induced cavity collapse or both in this region. This is reinforced by the high-resolution PSD in Figure 3 where at σ = 0.6, the spectra exhibit peaks at both 11.7 Hz (St = 0.12, shockwave-driven) and 21.5 Hz (St = 0.23, re-entrant jet-driven) with visual evidence observed in high-speed imaging for both hydrofoils.

The third mode (type 3) is evident in the spectrograms at $0.6 < \sigma < 0.9$, co-existing with type 2 for both hydrofoils. The type 3 mode is also seen to vary with σ as a power lower with an exponent of 3 but the trend differs between hydrofoils where $St_{3F} \approx 0.05\sigma^3+0.44$ and $St_{3R} \approx 0.2\sigma^3+0.43$ for the flexible and rigid, respectively. Identification of the tertiary mode is made evident in the power distribution maps below.

To gain spatial insight into the shedding behaviour, power distribution maps of identified shedding modes are shown in Figure 5. The maps are obtained by performing a FFT on the time series of each pixel and extracting the frequency specific power, then plotting the values to form a plot of distribution of power through the image. At σ = 0.8, both hydrofoils exhibit two shedding modes (type 2 and 3) of which the type 2 shedding occurs at similar frequencies of 37.7 and 37.4 Hz (St = 0.392 and 0.397, also shown in Figure 3) for the flexible and rigid hydrofoils, respectively. Power distributions reveal that this fundamental frequency is driven by shedding between s/6 and s/2 from the root for both hydrofoils.

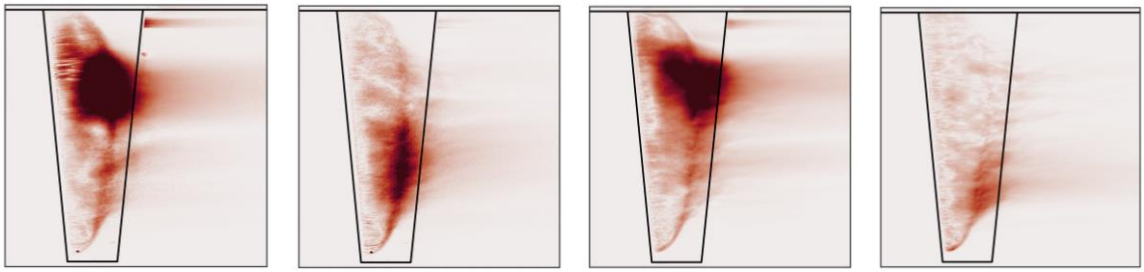

(a) Flexible: 37.7 Hz, St = 0.392 (b) Flexible: 44.4 Hz, St = 0.462 (c) Rigid: 37.4 Hz, St = 0.397 (d) Rigid: 49.9 Hz, St = 0.53

Figure 5 Power distribution of shedding events for the (a & b) flexible and (c & d) rigid hydrofoil with type 2 mode shown in (a) and (c) while a type 3 mode is shown in (b) and (d). All data is for σ = 0.8.

The tertiary mode (type 3) of each hydrofoil occurs at different frequencies coinciding with those observed in the normal force PSD (Figure 3) at 44.4 Hz (St = 0.462) and 49.9 Hz (St = 0.53) for the flexible and rigid hydrofoil, respectively. The power concentration of the tertiary mode is localized to the lower half of the span in contrast to the type 2 mode in the top half. Due to the principle spanwise bending deformations of the flexible hydrofoil, the type 3 mode power distribution extends further along the span than that of the rigid hydrofoil. High-speed imaging show that both the type 2 and 3 shedding modes are re-entrant jet driven.

With both hydrofoils exhibiting two shedding modes and power distributions showing they cover separate regions of the planform indicates the formation of two shedding events on the hydrofoil for a particular σ. The occurrence of the differing shedding events along the span is supported by the span-wise space-time plots in [8] and high-speed imaging. The formation of multiple span-wise shedding events is not observed at σ other than 0.8 as the cavity length, both stream-wise and span-wise, are incompatible with the hydrofoil span and, instead, result in an irregular break-off mechanism [22]. In the present study additional variations in spanwise geometry, hydrostatic pressure and hydroelastic response may also attribute to this behaviour.

Conclusions

Fluid-structure interaction is seen to have an effect on the cavity dynamics and induced normal force fluctuations experienced by a hydrofoil operating under cloud cavitation conditions. JTFA identified three shedding modes, type 1, 2 and 3, where the type 2 and 3 modes are seen to vary as a power law with σ. Power in the peak frequencies is seen to drop by approximately one order of magnitude with every 0.2 reduction in σ. Furthermore, it is shown that the rigid hydrofoil exhibits double the power of the flexible hydrofoil at the fundamental peak frequencies for σ between 0.6 and 0.8. However, the flexibility of the composite hydrofoil resulted in 3 times the power of that of the rigid at σ equal to 0.4, where the shedding mode has transitioned from type 2 to 1. The fundamental peak frequencies at each σ were not seen to vary significantly between hydrofoils, suggesting flexibility has more effect on the severity of cloud cavitation than its shedding frequency. Power distribution maps show the existence of two shedding modes (type 2 and 3) along the span of the hydrofoils that match those in the PSDs. The common

*Corresponding Author, Samuel Smith: ssmith18@utas.edu.au

type 2 mode frequency (37 Hz, St = 0.39) is seen to be due to shedding cavities on the upper half of the hydrofoil. The flexibility of the composite hydrofoil is seen to drop the type 3 mode frequency from 49 Hz (St = 0.52) to 42 Hz (St = 0.44) as well as change the spatial distribution of the secondary shedding across the bottom half of the span. The complex behaviour found under cavitation conditions indicates that any simple design assumptions applied to flexible hydrofoils may be not sufficient and a detailed analysis of these structures is required.

Acknowledgements

This project was supported by the University of Tasmania, the Defence Science and Technology Group, US Office of Naval Research (Dr. Ki-Han Kim, Program Officer) and ONR Global (Dr. Woei-Min Lin) through NICOP S&T Grant no. N62909-11-1-7013. The authors would like to acknowledge the assistance of Mr Steven Kent and Mr Robert Wrigley from the Australian Maritime College for their essential help with setting up and carrying out the experiments.

References

[1] Young, Y. L. (2008). *Fluid–structure interaction analysis of flexible composite marine propeller*s. Journal of Fluids and Structures. 24(6):799–818.
[2] Motley, M., Liu, Z., & Young, Y. (2009). *Utilizing fluid–structure interactions to improve energy efficiency of composite marine propellers in spatially varying wake.* Composite Structures. 90(3), 304-313.
[3] Turnock, S., Wright, A. (2000). *Directly coupled fluid structural model of a ship rudder behind a propeller.* Marine Structures. 13(1), 53-72.
[4] Young, Y. L. (2007). *Time-dependent hydroelastic analysis of cavitating propulsors*. Journal of Fluids and Structures, 23(2), 269-295.
[5] Akcabay, D. T., Chae, E. J., Young, Y. L., Ducoin, A., & Astolfi, J. A. (2014). *Cavity induced vibration of flexible hydrofoils.* Journal of Fluids and Structures, 49 (Supplement C), 463-484
[6] Akcabay, D. T., & Young, Y. L. (2014). *Influence of cavitation on the hydroelastic stability of hydrofoils.* Journal of Fluids and Structures, 49, 170-185.
[7] Callenaere, M., Franc, J.-P., Michel, J.-M., & Riondet, M. (2001). *The cavitation instability induced by the development of a re-entrant jet.* Journal of Fluid Mechanics, 444, 223-256.
[8] Smith, S., Venning, J., Brandner, P., Pearce, B., Giosio, D., & Young, Y. L. (2017). *Cloud cavitation behaviour on a hydrofoil due to fluid-structure interaction*. 17th International Symposium on Transport Phenomena and Dynamics of Rotating Machinery, Maui, Hawaii.
[9] Ganesh, H., Wu, J., & Ceccio, S. (2016). *Investigation of cavity shedding dynamics on a NACA0015 hydrofoil using time resolved x-ray densitometry*. 31st Symposium on Naval Hydrodynamics, ONR.
[10] Ganesh, H., Mäkiharju, S. A., & Ceccio, S. L. (2016). *Bubbly shock propagation as a mechanism for sheet-to-cloud transition of partial cavities.* Journal of Fluid Mechanics, 802, 37-78.
[11] Reisman, G., Wang, Y.-C., & Brennen, C. E. (1998). *Observations of shock waves in cloud cavitation.* Journal of Fluid Mechanics, 355, 255-283.
[12] Venning, J., Giosio, D., Smith, S., Pearce, B. & Brandner, P. (2018). *The influence of nucleation on the spectral content of cloud cavitation about a hydrofoil.* The 10th International Symposium on Cavitation, Baltimore, Maryland, accepted paper.
[13] De Graaf, K. L., Brandner, P. A., & Pearce, B. W. (2017). *Spectral content of cloud cavitation about a sphere*. Journal of Fluid Mechanics, 812, R1.
[14] Venning, J., Smith, S., Brandner, P., Giosio, D., & Pearce, B. (2017). *The influence of nuclei content on cloud cavitation about a hydrofoil*. 17th International Symposium on Transport Phenomena and Dynamics of Rotating Machinery, Maui, Hawaii.
[15] Avellan, F., Dupont, P., & Ryhming, I. L. (1988). *Generation mechanism and dynamics of cavitation vortices downstream of a fixed leading edge cavity.* 17th Symposium on Naval Hydrodynamics, Berkeley, California.
[16] Kjeldsen, M., Arndt, R. E., & Effertz, M. (2000). *Spectral characteristics of sheet/cloud cavitation.* Journal of Fluids Engineering, 122(3), 481-487.
[17] Kawakami, D. T., Fuji, A., Tsujimoto, Y., & Arndt, R. (2008). *An assessment of the influence of environmental factors on cavitation instabilities*. Journal of Fluids Engineering, 130(3).
[18] Zarruk, G. A., Brandner, P. A., Pearce, B. W., & Phillips, A. W. (2014). *Experimental study of the steady fluid–structure interaction of flexible hydrofoils.* Journal of Fluids and Structures, 51, 326-343.
[19] Brandner, P., Lecoffre, Y., & Walker, G. (2007). *Design considerations in the development of a modern cavitation tunnel*. 16th Australasian Fluid Mechanics Conference, Gold Coast, Australia.
[20] Welch, P. (1967). *The use of fast Fourier transform for the estimation of power spectra: a method based on time averaging over short, modified periodograms*. IEEE Transactions on audio and electroacoustics, 15(2), 70-73.
[21] Smith, S., Pearce, B., Brandner, P., Clarke, D., Moreau, D., & Xue, Y. (2016). *Steady and unsteady loads acting on a hydrofoil immersed in a turbulent boundary layer.* 20th Australasian Fluid Mechanics Conference, Perth, Australia.
[22] Kawanami, Y., Kato, H., & Yamaguchi, H. (1998). *Three-dimensional characteristics of the cavities formed on a two-dimensional hydrofoil.* Third International Symposium on Cavitation. Grenoble, France.

*Corresponding Author, Samuel Smith: ssmith18@utas.edu.au